ADVANCED FUNCTIONAL MATERIALS
www.afm-journal.de

In Situ Electrical Characterization of Anatase TiO_2 Quantum Dots

Johanna Engel, Sean R. Bishop, Lionel Vayssieres, and Harry L. Tuller**

A novel method for performing in situ characterization of the electrical properties of pristine, ultrafine nanopowders is reported. A modified dilatometer, with a spring-loaded push rod and electrodes, allows for the simultaneous monitoring of the packed nanopowder's lateral displacement as well as its complex impedance spectroscopy as a function of temperature within a controlled environment. Anatase TiO_2 quantum dots of 2 nm diameter, on average, are examined and found to simultaneously shrink and become more resistive upon initial heating. The resistance changes by approximately 3 orders of magnitude upon heating, associated with the desorption of adsorbed water, demonstrating the need for sample preconditioning. Subsequent electrical resistivity measurements, as a function of oxygen partial pressure, over approximately 40 orders of magnitude, at temperatures between 300 °C and 400 °C, exhibit nearly 9 orders of magnitude change in conductivity. The data are consistent with a Frenkel-based defect disorder model characterized by an enthalpy of reduction of 5.5 ± 0.5 eV.

1. Introduction

Nanostructured materials commonly offer enhanced performance associated with their high surface to volume ratios, high interface densities and/or quantum-confinement effects. Many processing routes have been reported for fabricating nano-sized precursor powders, fibers, rods, etc. Superior performance has been reported in applications such as gas sensors, fuel cells, and photoelectrochemical (PEC) cells, to name a few. For example, nanostructured n-type semiconducting metal oxide gas sensors commonly offer orders of magnitude higher sensitivity due to more efficient modulation of the conductive core by the induced space charge resulting from chemisorption of gas molecules.[1,2] Nanostructured electrodes in solid oxide fuel cells enable reduction of the operation temperature as the increase in reaction sites compensates for slow reaction kinetics.[3] Similarly, nanostructured photo-electrodes in dye sensitized solar cells (DSSCs) and PEC cells improve performance by up to three orders of magnitude compared to thin film or bulk electrodes.[4–7] Additionally, in a PEC cell, light absorption is improved due to increased scattering[8] and charge separation issues are overcome as a result of shorter charge carrier path lengths.[9] Finally, quantization effects at the nanoscale allow bandgap tuning, further enabling engineering of the electronic properties of materials to achieve enhanced device performance.[10]

While the implementation of nanomaterials is highly advantageous in many applications, what is less clear is the impact of nanomorphology on the materials' inherent properties, such as its defect structure and electrical conductivity, as well as the role of processing conditions in influencing these properties. Typically, nanomaterials are prepared by a wide variety of methods, followed by integration into a device and followed, in turn, by performance testing, with minimal characterization of the nanomaterial itself. While this procedure quantifies the overall enhancement of specific device characteristics by the nanomaterials, it lacks the ability to probe how processing routes change the nanomaterial's inherent properties, as well as requiring a final device for characterization. For example, nanostructured copper (II) oxide-based hydrogen gas sensors have shown several fold differences in sensitivity as a result of different nanostructures resulting form similar processing routes.[11] Nanorods, urchin-like, and fiber-like structures were produced by microwave- assisted synthesis, only varying bases or solvents. Nevertheless, they each showed distinctly different sensor response.[12] While electrical testing of full sensor devices highlights the optimum nanostructure, it falls short of explaining why or how this structure is superior, as it is unclear whether increases in performance are solely due to increased surface area (or exposed crystallographic planes) and not fundamental changes in, for example, the electron/hole density. For instance, recent reports demonstrated the effect of nanoparticle size on the orbital character,[13] surface chemistry,[14] electron transfer[15] and efficiency[16] of large bandgap oxide semiconductors, triggering interests on the relation between

J. Engel, Dr. S. R. Bishop, Prof. H. L. Tuller
Department of Materials Science and Engineering
Massachusetts Institute of Technology
77 Massachusetts Avenue, Cambridge, MA 02139, USA
E-mail: tuller@mit.edu
Prof. S. R. Bishop
International Institute for Carbon Neutral
Energy Research (WPI-I2CNER)
Kyushu University
I2CNER Bldg. 423, 744 Motooka, Nishi-ku Fukuoka 819–0395, Japan
Prof. L. Vayssieres
International Research Center for Renewable Energy
State Key Laboratory of Multiphase Flow in Power Engineering
School of Energy & Power Engineering
Xian Jiaotong University
Room 1208, North 2 Bldg No. 28, Xianning West Rd, Xian, Shaanxi
710049, P. R. China
E-mail: lionelv@xjtu.edu.cn

DOI: 10.1002/adfm.201400203

(interfacial) electronic structure and nanodevice optimization and performance.

Detailed characterization of the electrical properties of nano building blocks prior to their implementation into nanodevices is of crucial importance for: 1) the fundamental knowledge of conductivity and conduction mechanisms for pure or doped nanostructures as well as the effect of non-stoichiometry on charge carrier concentration, 2) detection of variations in material properties due to processing routes, and 3) tuning the properties of nanomaterials to optimize them prior to their implementation and testing, thereby saving time in the refinement process and offering engineered opportunities for efficiency optimization.

In this article, a novel in-situ characterization technique for as produced nanopowders is presented. Simultaneously, the electrical properties and mechanical rearrangement of the particles during annealing are characterized and correlated.

2. Results and Discussion

Electrical measurements on lightly compacted nanopowders, contained in a silica or alumina crucible, were performed using a modified dilatometer setup, whereby the spring loaded pushrod normally used to measure specimen length was used in this case for length measurement, powder retention, and electrode support (**Figure 1**). The chamber allowed for temperature and oxygen partial pressure (pO_2) control.[17] In this study, anatase TiO_2 nanopowder, consisting of quantum dots with an average diameter of 2 nm, was investigated.

2.1. Crystal Structure and Morphology

The as-prepared TiO_2 quantum dots were found by powder X-ray diffraction (XRD) to solely exhibit the anatase phase (**Figure 2**). Peak broadening due to small crystallite size obscures individual peaks in close proximity to each other. Using line profile analysis and the Scherrer equation, an average crystallite size of 2 ± 2 nm and a microstrain of 1.3% were obtained. Rietveld refinement confirmed the 2 nm average crystallite size and ruled out traces of the rutile phase. The shoulder of the most intense peak and the small peak at 44° 2-theta are shifted compared to the rutile reference pattern and neither of their relative intensities, nor their peak broadening, agrees with the rutile reference pattern or the peak broadening of the anatase peaks, respectively. Following a 500 °C annealing treatment for 3 h,

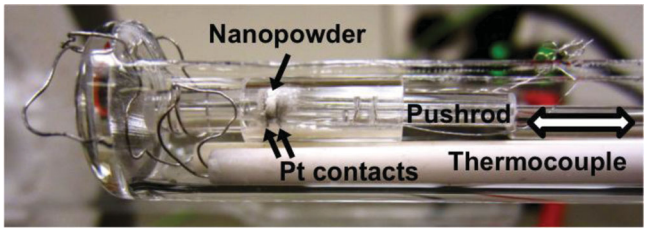

Figure 1. Nanopowder measurement arrangement, for simultaneous dilatometry and electrochemical impedance spectroscopy (EIS) measurements.

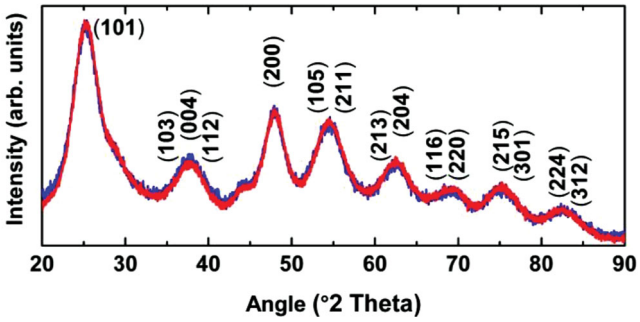

Figure 2. Indexed powder X-ray diffraction patterns before (blue) and after heat treatment (red) at 500 °C. Anatase peaks of 4% or greater relative intensity are indicated (JCPDS No. 00–021–1272).

the powder showed no detectable change in phase or crystallite size (Figure 2, red pattern). Transmission electron microscopy (TEM) analysis (Figure S1, Supporting Information) confirmed a spherical morphology and the dimension of the TiO_2 quantum dots.

2.2. Preconditioning: Dilatometry and Resistance

During the initial heating step, rather than the expected thermal expansion, an overall shrinkage of 6% was observed, along with a corresponding increase in resistance. In **Figure 3**a, the change in linear dimensions is reported in response to step changes in temperature. An initial expansion is observed with each temperature step, followed thereafter by a longer-term isothermal shrinkage. At the same time, an overall increase in resistance (measured by EIS, discussed later) is observed, with a rapid initial decrease in resistance followed by a long-term increase following heating from 300 °C and 400 °C, as shown in Figure 3b. During the 400 °C anneal, sample resistance and expansion ultimately reach near constant values with subsequent temperature changes below 400 °C resulting in a reversible thermal expansion response, although a small level of irreversible contraction continues to be observed for heat treatments above 400 °C (Figure 3c). Following the initial 400 °C heat treatment, the room temperature resistance increases irreversibly by over three orders of magnitude (Figure 3d). Subsequent measurements, however, remain reversible and reproducible as temperature or oxygen partial pressure is varied.

A large degree of shrinkage and an increase in resistance was observed upon the initial heating cycle of the as prepared powder. While shrinkage might be due to inter particle rearrangement into a denser structure, the resistance would not be expected to increase by orders of magnitude. Instead, one may consider a more likely scenario based on a change in the surface chemistry of the nanopowder upon heating. As a consequence of preparing this powder via an aqueous route, without surfactant, structural water molecules and hydroxyl ions remain at the oxide surface. Adsorbed water is known to conduct protons on the surface of oxides,[18,19] and upon heating, the water desorbs, resulting in an increase in resistance due to a change in conduction mechanism from surface protonic to a bulk transport mechanism. The large shrinkage detected by dilatometry is consistent with water loss as the source of the

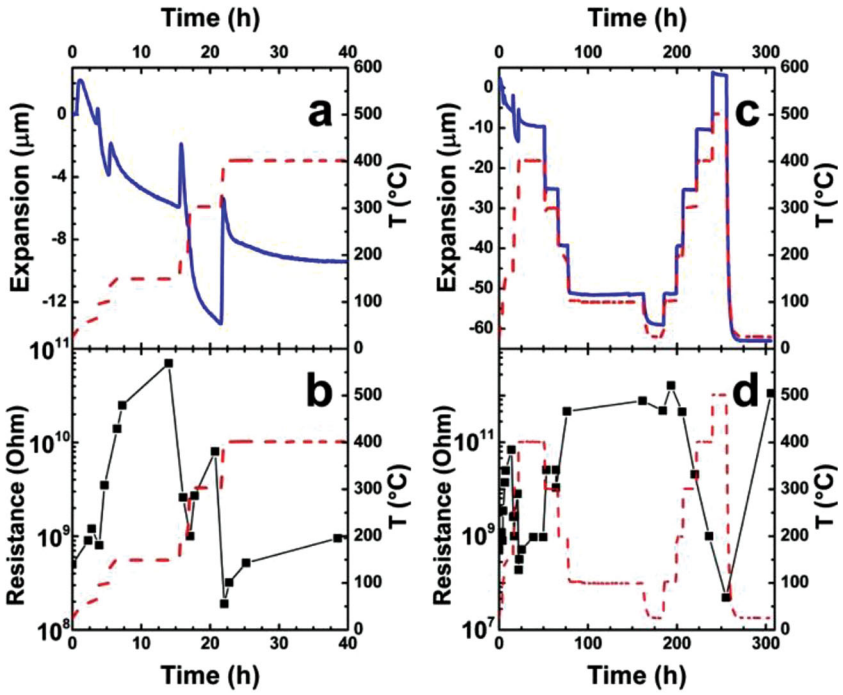

Figure 3. Expansion (blue line) and change in resistance (black solid squares) of as prepared TiO_2 during the first heating (a,b) and subsequent cooling and heating steps (c,d). The red dashed line indicates temperature profiles.

observed changes in resistance. Preconditioning facilitated the reproducibility of the EIS measurements, and, as discussed below, in-situ characterization of bulk TiO_2 defect equilibria and electrical transport properties. Interestingly, preconditioning did not induce particle coarsening as indicated by the average crystallite size remaining at 2 nm even following annealing the powder at 500 °C. Furthermore, the powder did not transition to the thermodynamically stable rutile phase. For anatase particles pressed into thin disks, this transition can begin at temperatures as low as 400 °C and concludes at 600 °C, by which time the particles have coarsened by one order of magnitude.[20] In another study, slow particle coarsening for 2 nm loose CeO_2 nanopowder was attributed to oxygen surface defects and the possibility of hydroxide groups on the surface.[21] Here, either surface defects or hydroxide groups may have stabilized the 2 nm anatase particles during preconditioning and EIS measurements.

2.3. Equilibrium Electrical Measurements

EIS measurements were performed as a function of temperature and pO_2 in order to identify the source of the charge carriers in the TiO_2 nanopowder. **Figure 4**a shows the impedance spectra measured in air as a function of temperature and Figure 4b shows similar spectra obtained as a function of pO_2 measured at 400 °C. The spectra are characterized by a somewhat depressed semicircle ($n_q = 0.83 \pm 0.03$) at higher frequencies (typically associated with bulk impedance), followed by a "tail" at low frequency (associated with particle-to-particle impedance). The deviation of the n_q value (exponent on the constant phase element resistance) from 1 for a perfect capacitor, may arise from the porosity of the lightly compacted nanopowder.[22] The porosity for a powder with 2 nm particles is expected to be between 60–70%. The particle resistance was extracted from the so-called high frequency arc, which intersects the origin at its upper frequency end, by fitting an equivalent circuit model consisting of a resistor and constant phase element in parallel to the spectra. As expected for an n-type semiconducting material, the resistance decreases with increasing temperature for a given partial pressure of oxygen (Figure 4a) and increases with increasing pO_2 (Figure 4b). The resulting conductivities are plotted in **Figure 5** and **6** as a function of pO_2 and reciprocal temperature with the data in Figure 5 showing a remarkable nine orders of magnitude change in conductivity at 300 °C with change in pO_2. The absolute conductivity is lower by one to two orders of magnitude compared to the literature values for single crystalline TiO_2[23] and densified nanocrystalline anatase (35 and 70 nm).[24,25] Porosity of the loose powder can only account for a 30% error in conductivity. As the quantum dots are only 2 nm in diameter, their point of contact has a miniscule cross section and as the particles are not sintered, there is no necking between them. This results in current constriction, as the electrons move through the bottleneck between the particles. There is no space charge barrier for the electrons to overcome, as this would have resulted in a large capacitative contribution, which

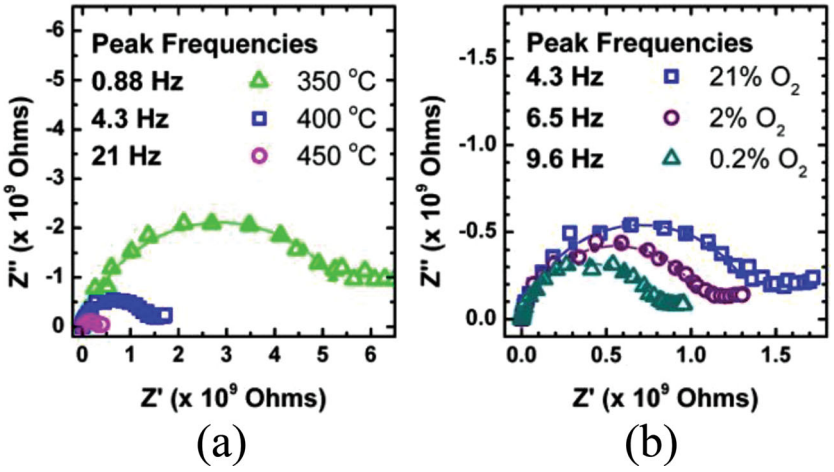

Figure 4. Complex impedance spectra showing measured data points (open symbols) and the result of equivalent circuit fitting to high-frequency data (connected filled symbols). The spectra were obtained for TiO_2 nanopowder following pre-conditioning at a) constant partial pressure of oxygen ($pO_2 = 0.21$ atm) and b) constant temperature of 400 °C.

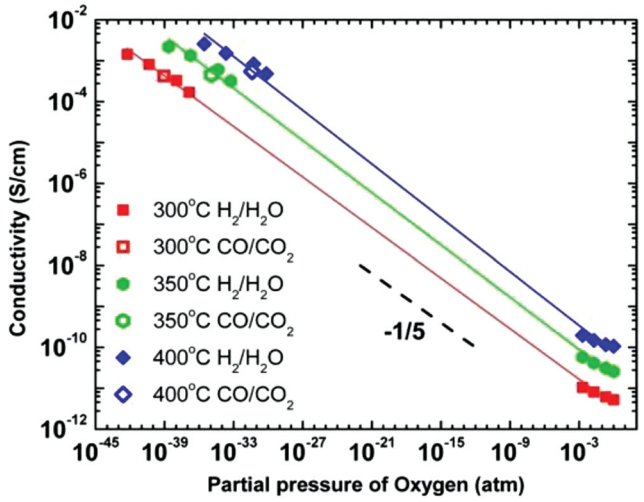

Figure 5. The conductivity of TiO_2 nanopowder as a function of pO_2 for several isotherms. The gas mixtures used to attain low pO_2 are distinguished by specified symbols: $H_2/H_2O/N_2$ (filled symbols) and CO/CO_2 (open symbols). An approximate −1/5 power law is observed for each isotherm, with slopes of −0.21, −0.21, and −0.22 and correlation coefficients of 0.99973, 0.99951, and 0.99899 for the linear fits at 300 °C, 350 °C, and 400 °C, respectively.

is not visible in the impedance spectra. However, this constriction to the flow of electrons explains the overall lower effective conductivity of these packed particles. It also explains the low frequency "tail," which scales in impedance with the high frequency semicircle at different temperature and partial pressure conditions. Therefore, both are subject to the same activation energy and pertain to the same transport mechanism, that being transport through the grain and not resulting from an interfacial effect.

More important than the absolute values are the trends revealed in this study. Linear fits to the isothermal data (Figure 5) reveal an approximate −1/5 power dependence of log conductivity on log pO_2. These results are discussed below in terms of defect equilibrium models describing mechanisms associated with loss of oxygen in TiO_2 upon reduction in pO_2 and/or increase in temperature. In Figure 6, an Arrhenius plot of conductivity for the four isobaric conditions at high pO_2 is shown. The slopes of the straight-line fits to the data yield the reported activation energy, E_a, in the figure, with average value 1.1 ± 0.1 eV, as defined by Equation (1).

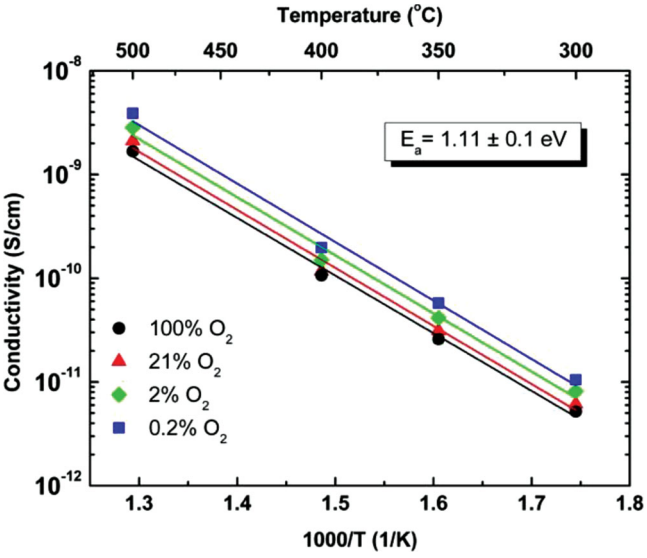

Figure 6. Arrhenius isobaric plot of the conductivity, revealing an average activation energy, E_a, of 1.1 ± 0.1 eV at high pO_2.

$$\sigma = \sigma_0 \exp\left(\frac{-E_a}{kT}\right) \quad (1)$$

Here, σ is conductivity, σ_0 a pre-exponential constant; k is Boltzmann's constant and T is the absolute temperature.

While many studies of the defect equilibria of TiO_2 are reported, conflicts remain regarding the dominant intrinsic ionic defect disorder (i.e., Schottky vs. Frenkel), with indications that structure and processing routes may play important roles.[23–27] In the ensuing discussion, the defect equilibria relationships for both defect types are presented and analyzed with respect to the electrical data obtained in this study.

Upon reduction of TiO_2 in low pO_2, oxygen is released, and in one scenario, lattice sites are annihilated as titanium interstitials are formed as described in terms of Kröger-Vink notation in Equation (2), with the corresponding mass action equation below it in Equation (3).

$$Ti_{Ti}^{x} + 2O_O^{x} \leftrightarrow Ti_i^{\bullet\bullet\bullet\bullet} + 4e' + O_{2(g)} \quad (2)$$

$$\left[Ti_i^{\bullet\bullet\bullet\bullet}\right] n^4 p_{O_2} = K_{\text{reduction}}^{F} = K_0^{F} \exp\left(\frac{-H_{\text{red}}^{F}}{kT}\right) \quad (3)$$

where Ti_{Ti}^{x}, O_O^{x}, $Ti_i^{\bullet\bullet\bullet\bullet}$, and e' are titanium ions on titanium sites, oxygen ions on oxygen sites, fully ionized titanium interstitials with a quadruple positive charge (with respect to the lattice) and electrons, respectively. In the mass action equation, $[Ti_i^{\bullet\bullet\bullet\bullet}]$ and n are charge carrier concentrations of titanium ion interstitials and electrons, respectively. $K_{\text{reduction}}^{F}$ is the equilibrium constant for the formation of titanium interstitials in a reducing atmosphere. K_0^{F} is a pre-exponential term including the entropy of reduction and H_{red}^{F} is the enthalpy of reduction for the Frenkel-like defect disorder. Under reducing conditions, the predominant charge carriers are expected to be titanium interstitials and electrons, so that the charge neutrality condition can be estimated by

$$n = 4\left[Ti_i^{\bullet\bullet\bullet\bullet}\right] \quad (4)$$

Since electrons are significantly more mobile than ions, the conductivity, σ, will be dominated by the former species through the following equation

$$\sigma = nq\mu_e \quad (5)$$

where q is the charge of an electron and μ_e is electron mobility. Substituting Equation (4) into Equation (3), and solving for n yields the following pO_2 dependence (Equation (6)), which corresponds to the conductivity dependence observed in Figure 5 (see Equation (5)).

$$n = \left(4K_0^{\mathrm{F}}\right)^{1/5} \exp\left(\frac{-H_{\mathrm{red}}^{\mathrm{F}}}{5kT}\right)\left(p_{\mathrm{O}_2}\right)^{-1/5} \quad (6)$$

On the other hand, if we assume the formation of oxygen vacancies, instead of titanium interstitials, upon reduction, one can define the following reaction (Equation (7)) and its corresponding mass action equation (Equation (8)).

$$\mathrm{O}_{\mathrm{O}}^{x} \leftrightarrow V_{\mathrm{O}}^{\cdot\cdot} + 2e' + \frac{1}{2}\mathrm{O}_{2(g)} \quad (7)$$

$$\left[V_{\mathrm{O}}^{\cdot\cdot}\right] n^2 p_{\mathrm{O}_2}^{1/2} = K_{\mathrm{reduction}}^{\mathrm{S}} = K_0^{S}\exp\left(\frac{-H_{\mathrm{red}}^{\mathrm{S}}}{kT}\right) \quad (8)$$

where $V_{\mathrm{O}}^{\cdot\cdot}$ is a doubly positive charged (with respect to the lattice) oxygen vacancy. In Equation (8), $[V_{\mathrm{O}}^{\cdot\cdot}]$ is the oxygen vacancy concentration. $K_{\mathrm{reduction}}^{\mathrm{S}}$ is the equilibrium constant for the formation of oxygen vacancies in a reducing atmosphere. K_0^{S} is a pre-exponential term including the entropy of reduction and $H_{\mathrm{red}}^{\mathrm{S}}$ is the enthalpy of reduction for the Schottky-like defect disorder.

Under reducing conditions, the predominant charge carriers are now expected to be oxygen vacancies and electrons and the following neutrality condition holds.

$$n = 2\left[V_{\mathrm{O}}^{\cdot\cdot}\right] \quad (9)$$

Substitution of Equation (9) into Equation (8), and solving for n yields the following pO_2 dependence for the electron concentration (Equation (10)).

$$n = \left(2K_0^{\mathrm{S}}\right)^{1/3} \exp\left(\frac{-H_{\mathrm{red}}^{\mathrm{S}}}{3kT}\right)\left(p_{\mathrm{O}_2}\right)^{-1/6} \quad (10)$$

Given the close agreement of the data reported in Figure 5 to a −1/5 power law dependence of conductivity on pO_2, the titanium interstitial model is clearly supported. Interestingly, with the ability to study powder specimens, equilibrium appears to be attained at temperatures considerably below those required for pressed ceramic disks (450 °C), which Knauth and coworkers obtained by sintering nanopowders with average particle size of 70 nm.[25] Furthermore, Knauth et al. established a −1/6 power law between 450 °C and 600 °C and only observed the −1/5 power dependence on pO_2 between 600 °C and 700 °C for these pellets.

Under isobaric conditions, the previous treatment of Equations (3) yields the following relationship.

$$\sigma = \left(q\mu_{\mathrm{e}}\right)\left(4K_0^{\mathrm{F}}\right)^{1/5} \exp\left(\frac{-H_{\mathrm{red}}^{\mathrm{F}}}{5kT}\right) \quad (11)$$

Given Equation (11), the activation energy in Figure 6 is equal to $\left(H_{\mathrm{red}}^{\mathrm{F}}/5\right)$ (assuming mobility is temperature independent[28]) yielding $H_{\mathrm{red}}^{\mathrm{F}} = 5.5 \pm 0.5$ eV. This value is only half that of the enthalpy of reduction determined for pressed ceramic pellets of anatase or rutile bulk material.[29] The removal of surface oxygen in ceria has been shown to be much less energetically costly than the removal of bulk oxygen.[30] In the case of the nanoparticulate powder, a very large fraction of the oxygen resides near the surface, thus enabling the easier removal of oxygen from the particles as reflected by the lower enthalpy of reaction. Furthermore, a space charge model, proposed to explain the electrical behavior of some nanocrystalline materials, would predict a systematic decrease in space charge width with increasing magnitude of conductivity (here as much as 9 orders of magnitude) as the pO_2 is decreased with corresponding changes in the pO_2 dependence of the conductivity.[31] No such changes are observed in this study.

One may further question if the measured impedance truly corresponds to the "bulk" properties of the nanoparticles and not to simple surface adsorption/desorption effects as reported for semiconducting metal oxide sensor materials such as SnO_2.[32] The interpretation that this change in resistance is due to a change in the oxygen stoichiometry of the TiO_2 particles is supported by the fact that the resistance was independent of the gas mixture used to set the pO_2 of the gas. Thus, a CO/CO_2 mixture, used to fix the partial pressure of oxygen at various temperatures (Figure 5), resulted in specimen resistances in good agreement with those obtained previously while streaming $H_2/H_2O/N_2$ gas mixtures. If the resistance change were dependent on the nature of the gas molecules chemisorbing on the surface, very different values of resistance would be expected. In addition, no sensitivity maximum as a function of temperature was observed, a feature quite typical of sensors operating on the basis of a chemisorption process.[33,34] Furthermore, the long equilibration times on the order of days (see Figure S2, Supporting Information) required following a change in pO_2 suggest bulk diffusion limited kinetics.

The relative dielectric constant, ε_{r}, for the nanopowder can also be calculated from the EIS measurements. Using the values for resistance, R, the constant phase element, Q, and n_{q}, one can determine the capacitance (Equation (12)). ε_{r} is then determined from the definition of capacitance, C (Equation (13).

$$C = \left(R^{1-n_{\mathrm{q}}}Q\right)^{1/n_{\mathrm{q}}} \quad (12)$$

$$\varepsilon_{\mathrm{r}} = \frac{C}{\varepsilon_0}\frac{l}{A} \quad (13)$$

where ε_0 is the vacuum permittivity and l and A are the thickness of the sample and the area of the electrodes, respectively. Using the values from the fits in Figure 4, one arrives at a relative dielectric constant of 60, 55, and 54 for EIS measurements at 350 °C, 400 °C, and 450 °C, respectively, in a pO_2 of 0.21 atm (Figure 4a). A relative dielectric constant of 55 is derived for all measurements at 400 °C at different pO_2's (Figure 4b). Small variations in this value are expected due to changes in the geometric factor, $l/lA - A$, with changes in temperature, this being particularly the case given that the powder is loosely packed and therefore not a dense, bulk specimen. These values are in close agreement with the value of 55 already reported for the relative dielectric constant of polycrystalline thin films of anatase, with a thickness ranging from 80 to 120 nm.[35] Together with the higher resistance due to constriction of the flow of electrons between particles, the as expected capacitance value for anatase explains the low peak frequency values observed in Figure 4. The peak frequency is defined as $1/(RC)$

and therefore a higher resistance with a constant capacitance will result in a lower peak frequency value.

3. Conclusions

Nanopowders are rarely characterized electrically prior to being incorporated into a device. In this study, in-situ characterization of lightly packed nanopowders, in a modified dilatometer apparatus, was demonstrated. This approach enables the study of the electrical properties of nanopowders and furthermore, provides insight as to how non-stoichiometry of oxide powders influences their conductivity by changes in carrier concentration and/or transport mechanism. In the case of the anatase TiO_2 nanoparticles studied here, it was determined that oxygen loss is governed by the generation of fully ionized titanium interstitials and accompanying electrons. Moreover, this in-situ characterization detects variations in samples due to their processing routes, which can have a major impact on the product's final properties. In the TiO_2 case study, preconditioning, i.e., a full heating cycle, was required to reach equilibrium values at given temperatures and pO_2's, thereby eliminating potential spurious effects related to the processing procedure, e.g., the effect of adsorbed water. This case study presents a method to characterize nanomaterials prior to their implementation into functional devices, thereby enabling determination of electrical conduction mechanisms as well as establishing the material's equilibrium state in a given atmosphere regardless of processing route. It furthermore demonstrates the ability to modify and control defect concentrations and electrical conductivity in particles as small as 2 nm in diameter by many orders of magnitude.

4. Experimental Section

Powder Preparation and Characterization: Stable aqueous suspensions of anatase TiO_2 quantum dots, with an average diameter of 2 nm, were produced at 60 °C without surfactant, following a pristine hydrothermal synthesis route. This involved the controlled olation and oxolation of metal ion aquo-hydroxo complexes, based on a general metal oxide thermodynamic stabilization strategy, described and illustrated in detail in reference.[36] Subsequently, powders were extracted by ultracentrifugation at low temperature and dried in air at room temperature. Electronic structure characterization was carried out at synchrotron radiation facilities[13] by X-ray absorption spectroscopy. TEM (Figure S1, Supporting Information) and powder XRD (Figure 2) were performed for the determination of average particle size and crystal phase prior to and following heat treatments.

In Situ Electrochemical Impedance Spectroscopy and Dilatometry: EIS measurements on lightly compacted nanopowders were performed using a modified dilatometer setup. The spring-loaded pushrod retaining the powder also maintained electrical contact to the sample electrodes and was used to measure lateral sample expansion. The initial sample dimensions were 8.33 mm in diameter (alumina crucible inner diameter) and 0.85 mm in height. Lateral expansion and contraction of the sample was measured continuously. Changes in dimensions were observed with changes in temperature. Thermal expansion of the sample holder containing the nanopowder, including the Pt electrical contacts, can be neglected as it only amounts to approximately 1% of the thermal expansion of the sample itself. Chemical expansion at constant temperature, due to changes in stoichiometry of the TiO_2 particles subsequent to changes in atmosphere, was not observed, as the dilatometer was not sensitive enough to record these minute changes. Mixtures of O_2/N_2, $H_2/H_2O/N_2$, and CO/CO_2, whose ratios and flow rates were adjusted by mass flow controllers, were used to fix the oxygen partial pressure (pO_2), ranging from oxidizing to highly reducing conditions, within the enclosed sample chamber. EIS measurements were performed with a Novocontrol Technologies Model Alpha-A Impedance Analyzer (Hundsangen, Germany) over the frequency range of 0.02 Hz to 1 MHz with an oscillation amplitude of 500 mV and no additional applied DC bias, thereby allowing for the isolation of bulk from interfacial contributions. The integration time was 0.5 sec for each data point, except at low frequencies, where it spanned at least one cycle. EIS was measured for temperatures of 20 °C to 500 °C and pO_2 from 1 to $\approx 10^{-40}$ atm. The conductivity was calculated as the reciprocal of resistivity, ρ.

$$\sigma = \frac{1}{\rho} = \frac{1}{R}\frac{l}{A} \tag{14}$$

R is the resistance determined by the fit to the impedance spectrum. The area is constant as it is set by the size of the electrodes containing the powder and the thickness was adjusted according to the dilatometry measurement.

Supporting Information

Supporting Information is available from the Wiley Online Library or from the author.

Acknowledgements

The authors acknowledge the Chesonis Family Foundation (MIT-2741836) and the National Science Foundation (DMR-09908627) for financial support of this study. This work made use of the MRSEC Shared Experimental Facilities at MIT, supported by the National Science Foundation under award number DMR-08–19762. J.E. thanks Dr. S. Speakman for assistance with the analysis of the XRD patterns. S.R.B. recognizes support from I^{2}CNER, supported by the World Premier International Research Center Initiative, MEXT, Japan. L.V. acknowledges support from the International Research Center for Renewable Energy, State Key Laboratory of Multiphase Flow in Power Engineering, Xi'an Jiaotong University, the Thousand Talents plan and the National Natural Science Foundation of China (No. 51121092).

Received: January 20, 2014
Revised: March 12, 2014
Published online: May 23, 2014

[1] A. Rothschild, H. L. Tuller, *J. Electroceram.* **2006**, *17*, 1005.
[2] I.-D. Kim, A. Rothschild, H. L. Tuller, *Acta Mater.* **2013**, *61*, 974.
[3] E. D. Wachsman, K. T. Lee, *Science* **2011**, *334*, 935.
[4] K. Shankar, J. I. Basham, N. K. Allam, O. K. Varghese, G. K. Mor, X. Feng, M. Paulose, J. A. Seabold, K.-S. Choi, C. A. Grimes, *J. Phys. Chem. C* **2009**, *113*, 6327.
[5] P. Yang, R. Yan, M. Fardy, *Nano Lett.* **2010**, *10*, 1529.
[6] M. Gratzel, *Nature* **2001**, *414*, 338.
[7] P. V. Kamat, *J. Phys. Chem. C* **2007**, *111*, 2834.
[8] S. W. Boettcher, J. M. Spurgeon, M. C. Putnam, E. L. Warren, D. B. Turner-Evans, M. D. Kelzenberg, J. R. Maiolo, H. A. Atwater, N. S. Lewis, *Science* **2010**, *327*, 185.
[9] N. Beermann, L. Vayssieres, S. Lindquist, A. Hagfeldt, *J. Electrochem. Soc.* **2000**, *147*, 2456.

[10] L. Vayssieres, C. Sathe, S. M. Butorin, D. K. Shuh, J. Nordgren, J. Guo, *Adv. Mater.* **2005**, *17*, 2320.
[11] D. P. Volanti, A. A. Felix, M. O. Orlandi, G. C. Whitfield, D.-J. Yang, E. Longo, H. L. Tuller, J. A. Varela, *Adv. Funct. Mater.* **2013**, *23*, 1759.
[12] D. P. Volanti, A. G. Sato, M. O. Orlandi, J. M. C. Bueno, E. Longo, J. Andrés, *ChemCatChem* **2011**, *3*, 839.
[13] L. Vayssieres, C. Persson, J.-H. Guo, *Appl. Phys. Lett.* **2011**, *99*, 183101.
[14] L. Vayssieres, *J. Phys. Chem. C* **2009**, *113*, 4733.
[15] C. X. Kronawitter, J. R. Bakke, D. Wheeler, W. C. Wang, C. L. Chang, B. R. Antoun, J. Z. Zhang, J. H. Guo, S. F. Bent, S. S. Mao, L. Vayssieres, *Nano Lett.* **2011**, *11*, 3855.
[16] C. X. Kronawitter, I. Zegkinoglou, C. Rogero, J.-H. Guo, F. J. Himpsel, S. S. Mao, L. Vayssieres, *J. Phys. Chem. C* **2012**, *116*, 22780.
[17] A recent publication describing the monitoring of the densification of a polycrystalline ceramic within a dilatometer by impedance spectroscopy [R. Muccillo, E.N.S. Muccillo, *J. Euro. Ceram. Soc.* **2013**, *33*, 515] was brought to the attention of the authors by one of the reviewers. While outwardly similar to the arrangement described here, in that study, there was no attempt to characterize the electrical properties of an ensemble of loose nanoparticles, but rather a ceramic that had been isostatically pressed at 210 MPa followed by flash sintering.
[18] H. J. Avila-Paredes, E. Barrera-Calva, H. U. Anderson, R. A. De Souza, M. Martin, Z. A. Munir, S. Kim, *J. Mater. Chem.* **2010**, *20*, 6235.
[19] C. Tandé, D. Pérez-Coll, J. C. Mather, *J. Mater. Chem.* **2012**, *22*, 11208.
[20] Q. Wu, D. Li, Y. Hou, L. Wu, X. Fu, X. Wang, *Mater. Chem. Phys.* **2007**, *102*, 53.
[21] B. B. T. Neltner, *Ph.D.* Thesis Massachusetts Institute of Technology, Cambridge, MA, **2010**.
[22] D. I. Raistrick, D. R. Franceschetti, J. R. Macdonald, in *Impedance Spectroscopy: Theory, Experiment, and Applications*, Vol. *2* (Eds: E. Barsoukov, J. R. Macdonald), John Wiley & Sons, Inc., Hoboken, NJ **2005**; pp 75–80, 118–128.
[23] M. K. Nowotny, T. Bak, J. Nowotny, *J. Phys. Chem. B* **2006**, *110*, 16270.
[24] P. Knauth, H. L. Tuller, *J. Appl. Phys.* **1999**, *85*, 897.
[25] A. Weibel, R. Bouchet, P. Knauth, *Solid State Ionics* **2006**, *177*, 229.
[26] M. K. Nowotny, T. Bak, J. Nowotny, *J. Phys. Chem. B* **2006**, *110*, 16283.
[27] M. K. Nowotny, T. Bak, J. Nowotny, *J. Phys. Chem. B* **2006**, *110*, 16292.
[28] M. K. Nowotny, L. R. Sheppard, T. Bak, J. Nowotny, *J. Phys. Chem. C* **2008**, *112*, 5275.
[29] J. Marucco, J. Gautron, P. Lemasson, *J. Phys. Chem. Solids* **1981**, *42*, 363.
[30] T. X. T. Sayle, S. C. Parker, C. R. A. Catlow, *Surf. Sci.* **1994**, *316*, 329.
[31] K.-R. Lee, J.-H. Lee, H.-I. Yoo, *Phys. Chem. Chem. Phys.* **2013**, *15*, 15632.
[32] A. Gurlo, R. Riedel, *Angew. Chem. Int. Ed.* **2007**, *46*, 3826.
[33] L. Zhang, J. Zhao, H. Lu, L. Li, J. Zheng, H. Li, Z. Zhu, *Sens. Actuators B* **2012**, *161*, 209.
[34] I.-D. Kim, A. Rothschild, B. H. Lee, D. Y. Kim, S. M. Jo, H. L. Tuller, *Nano Lett.* **2006**, *6*, 2009.
[35] R. Van de Krol, A. Goossens, J. Schoonman, *J. Electrochem. Soc.* **1997**, *144*, 1723.
[36] L. Vayssieres, *Int. J. Nanotechnol.* **2005**, *2*, 411.